Available online at www.CivileJournal.org

Civil Engineering Journal

(E-ISSN: 2476-3055; ISSN: 2676-6957)

Vol. 12, No. 05, May, 2026

Assessing the Relationship Between Groundwater Dynamics and Land Subsidence Using Time-Series SAR Data

Yehia Miky [1, 2*]

[1] *Department of Geomatics, Faculty of Architecture and Planning, King Abdulaziz University, Jeddah 21589, Saudi Arabia.*

[2] *Faculty of Engineering, Aswan University, Aswan 81542, Egypt.*

Received 28 March 2026; Revised 23 April 2026; Accepted 27 April 2026; Published 01 May 2026

Abstract

Groundwater is considered as the primary source of drinking and agricultural supply for most residents in Mecca region. However, data indicates that groundwater restore is substantially lower than the consumption rate, which results in a reduction in the quality of water and decline in groundwater levels. This, in turn, has resulted in surface subsidence, causing problems in infrastructure. The main aim of this research is to assess the correlation between groundwater dynamics and surface subsidence in the Mecca region using time-series SAR imagery. So, time series maps of land subsidence, along with the spatial distribution of long-term subsidence from 2016 to 2025, were generated. The results indicate that the basin experienced an average deformation velocity of less than 4 cm/year, with maximum subsidence reaching 15.2 cm in highly compressible soils. The analysis further shows that land subsidence generally increases with higher groundwater extraction rates. However, only two soil types (the Abbasah Formation and the diorite–pyroxenite unit) exhibited a substantial positive correlation between groundwater flow rate and subsidence ($R^2 = 0.67$). Quantitative analysis of the correlation helps water managers to take the necessary actions, such as identifying crop types, and irrigation methods, to preserve and sustain the Kingdom's water resources.

Keywords: Groundwater; SAR Imagery; Land Subsidence; Correlation; Mecca Region.

1. Introduction

Groundwater represents the largest global reservoir, as it contains over 98% of the world's available freshwater [1, 2]. It is essential for irrigation and drinking. However, over-exploration of groundwater can cause different environmental issues, like compaction of highly compressible soils [3, 4], which leads to land subsidence that is dangerous to human settlements, natural terrains, and groundwater sustainability in the long run. Land subsidence is a geological phenomenon that has environmental effects caused by the compaction and consolidation of underground soil layers, either through natural processes or human activities, consequently causing a reduction in the Earth's surface height [5]. With the acceleration of urbanization, land subsidence has emerged as a pressing global environmental problem. Extensive human-driven groundwater extraction caused severe land subsidence in many regions worldwide [2, 6-8]. Groundwater extraction in arid and semi-arid regions is more than a critical issue, where it often represents the main source of water for domestic, industrial, and agricultural.

Wadi Nu'man, located in the Mecca region in Saudi Arabia, holds significant hydrological importance, serving as a key source of agricultural water and domestic supply for the Makkah region [9, 10]. This area is undergoing rapid urban expansion in the main valley and its tributaries, with new residential zones emerging in recent years [11]. Residents of

* Corresponding author: yhhassan@kau.edu.sa

https://doi.org/10.28991/CEJ-2026-012-05-07

Wadi Nu'man and the surrounding communities depend primarily on groundwater for drinking and agricultural activities. However, current data indicates that groundwater recharge is considerably lower than the rate of extraction [12], leading to declining water levels and deteriorating water quality. These changes adversely affect both domestic and agricultural uses. Therefore, the region urgently requires not only a comprehensive water management and monitoring system, along with measures such as regulating crop types, optimizing irrigation methods, and managing cultivated areas, but also a way to accurately monitor the spatial and temporal vertical deformation associated with the over extraction of groundwater to ensure the long-term sustainability of water resources.

Traditional ground-based methods—such as triangulation and geodetic leveling—can deliver highly accurate measurements but are limited by sparse and unevenly distributed observation points, which hampers their effectiveness in capturing the regional patterns of land subsidence [6]. Recent technological developments in remote sensing, notably synthetic aperture radar (SAR), offer a rich suite of tools to detect time-dependent surface deformation up to millimeter-level accuracy [13-17]. Particularly interferometric synthetic aperture radar (InSAR), a significant branch of radar technology, has become indispensable for surface deformation monitoring because of its wide advantages, including wide coverage, the capability to monitor all-weather and during all-day [18], remarkable precision [19], and its applications across various fields [20-23]. Time-series InSAR was developed to overcome limitations of interferometric phase measurements, like spatial–temporal decorrelation and atmospheric delays [24, 25]. This makes it a preferred technique for land subsidence monitoring and has led to its widespread application [26, 27].

The InSAR interferometric phase consists of several components, including deformation, topographic, atmospheric, and noise-related phases. Therefore, extracting meaningful signals from the interferometric phase is very challenging [28]. One of the main approaches utilized to identify deformation signals is independent component analysis (ICA), which was introduced into InSAR research early in 2002 by Inglada & Adragna [29]. The advantages of ICA in extracting atmospheric artifacts and topographic residuals away from deformation components were demonstrated by Ballatore in 2006 [30]. Persistent Scatterer Interferometry SAR (PS-InSAR) is an advanced InSAR technique to monitor and analyze earth surface displacement with time series analysis with high accuracy [31]. Many researchers have applied deep learning to the field of InSAR phase filtering. For instance, MCR-PFNet, a novel InSAR interferometric phase filtering method based on deep learning, was presented by Wang et al. (2025) for complex noise and large gradient deformations [32]. Also, an optimal feature-based InSAR phase filtering framework using a convolutional neural network and mathematical morphology was presented in 2026 by Hamed et al. [33].

Different scholars have investigated the correlation between land subsidence and groundwater [18, 34-43]. For example, Chaussard et al. (2017), in their study about Santa Clara Valley in California, utilized ICA to analyze surface deformation [44]. In 2022, Lucknow Municipal Corporation region, the changes in groundwater levels were estimated by Awasthi et al. [45]. Some scholars investigated the hydraulic movement associated with groundwater extraction and its crucial role in explaining how aquifer systems can respond to the change in stresses and result in land subsidence [46-49]. For instance, the over-extraction of groundwater from the second confined aquifer in the Beijing Plain was the main factor of land subsidence there [46, 50]. In fact, over-exploration of groundwater results in a reduction in pore water pressure, which in turn leads to an increase in effective stress that causes soil compaction and land subsidence [51-53]. Akitaya and Aichi, in their research on aquifer system deformation, emphasized that trend-type subsidence consists of two components. The first is the transient responses that synchronize the changes in groundwater levels, whereas the second is independent from water level changes and comes from accumulated historical deformation residuals [54].

Despite the growing body of literature on SAR technologies and applications as well as in land subsidence in various urban and agricultural regions worldwide, limited research has investigated the spatiotemporal relationship between groundwater depletion and surface deformation in arid environments of western Saudi Arabia, particularly within the Wadi Nu'man Basin. Therefore, this study aims to address this research gap by integrating long-term Sentinel-1 time-series InSAR analysis with geological information and groundwater observations to evaluate subsidence dynamics within the study area. Therefore, the main objectives of this research are to analyze temporal variations in groundwater levels in the Mecca region, detect and quantify land surface subsidence using time-series SAR data, evaluate the spatial and temporal correlations between groundwater depletion and surface deformation, and identify high-risk zones where subsidence is closely associated with groundwater extraction.

The contributions of this research can be summarized as the following:

- Production of time-series maps of surface deformation and groundwater fluctuations in the Mecca region.
- Providing clear visual and analytical insights into subsurface and environmental dynamics related to different soil types.
- Identifying high-risk zones related to groundwater extraction and land subsidence.

The findings of this research will support more effective urban planning and groundwater management strategies, contributing to sustainable development goals in accordance with Saudi Arabia's Vision 2030 [55].

This paper begins by providing a brief introduction to the study, followed by a description of the methodology in Section 2. Then, the obtained results are presented in Section 3, where Section 4 discusses the obtained results, limitations, and future work. Finally, Section 5 displays the conclusions of this study.

2. Materials and Methods

2.1. Study Area

As shown in Figure 1, the Wadi Nu'man basin is located in the Mecca region, Saudi Arabia, and spans between the latitudes of 21°10'32.31" and 21°28'28.76" North and longitudes of 40°09'09.62" and 40°09'46.17" East. The surroundings of the basin are Wadi Al-Bagidi in the north, the heights of Al-Hada in the East, in the West Red Sea and Wadi Malkan is considered the southern boundary. Wadi Nu'man consists of eleven subbasins, which are Wadi Mujireish, Wadi Nu'man, Wadi Zubaydah, Wadi Ash Shadqa, Wadi Ash Shara, Wadi Tiftifan, Wadi Ya'ruj, Wadi Alaq, Wadi Tinaamah, Wadi Rahjan, and Wadi Arar. The most important characteristics of Wadi Nu'man subbasins are presented in Table 1. The Wadi Nu'man basin is characterized by distinctive natural features resulting from its mountainous terrain and extensive area. These features include varying elevations, slopes, and numerous small sub-basins. The basin also forms an extension of the residential and agricultural expansion of the city of Mecca. It has a ruggedness ratio of approximately 0.61, the elevation above sea level ranging from 350 to 2,500 meters. Its hydrological characteristics make it the eastern watershed of Mecca, classified at the sixth watershed level. Figure 2 shows the digital elevation model (DEM) along with the morphological characteristics of the basin.

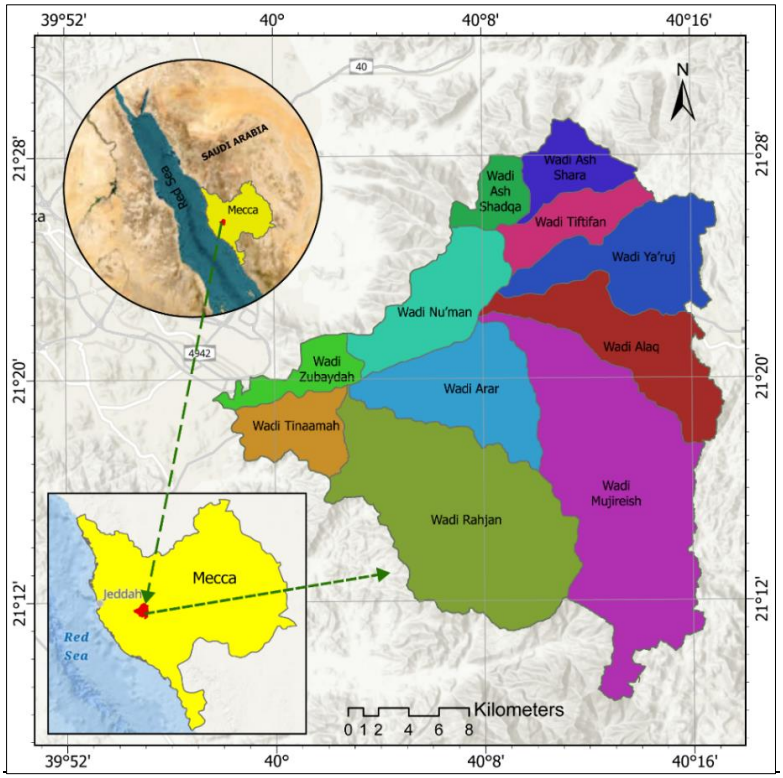

Figure 1. Location of Wadi Nu'man area

Table 1. The most important characteristics of Wadi Nu'man subbasins

Basin Name	Area (km^2)	Depth of ground water table (m)				Rate of flow of water (m^3/day)			
		Min.	Mean	Max.	S.D	Min.	Mean	Max.	S.D
Wadi Mujireish	172.96	0.04	35.12	65.72	5.86	0.29	97.04	786.69	55.85
Wadi Nu'man	50.69	0.00	18.79	45.56	12.50	0.01	138.25	1062.17	78.29
Wadi Zubaydah	20.04	0.00	18.68	54.42	11.71	8.04	202.44	722.49	139.97
Wadi Ash Shadqa	16.27	17.18	22.08	27.97	1.20	1.58	102.76	172.03	37.90
Wadi Ash Shara	25.53	15.82	20.44	22.11	0.52	8.70	145.27	175.38	21.55
Wadi Tiftifan	27.45	0.04	18.23	28.70	3.37	23.67	200.12	470.90	45.59
Wadi Ya'ruj	59.87	0.55	22.04	36.73	6.36	1.19	207.34	357.96	66.14
Wadi Alaq	62.73	0.34	28.56	42.28	9.06	2.48	121.83	352.09	84.87
Wadi Tinaamah	30.39	0.13	26.37	69.80	8.77	0.96	286.51	550.23	96.24
Wadi Rahjan	152.52	1.08	33.64	53.68	6.03	0.14	66.18	323.68	53.71
Wadi Arar	63.84	0.02	18.60	50.71	9.76	0.07	123.37	775.21	131.14

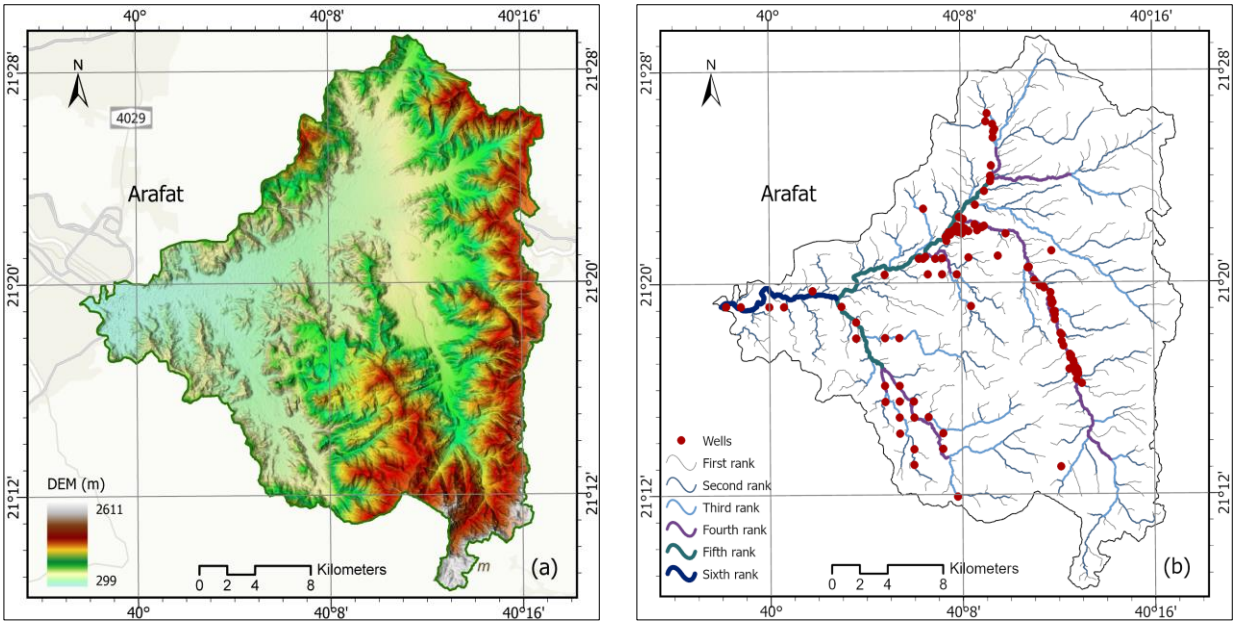

Figure 2. The morphological characteristics of the study area: (a) DEM; (b) the order of streams

Rainfall is considered as the primary source of groundwater replenishment in Wadi Nu'man basin, where rainwater infiltrates through cracks and fissures in the rocks to reach the aquifer, helping to offset daily withdrawals. Rainfall in the basin exhibits significant variability in both amount and timing and often occurs abruptly, leading to flash floods, particularly in rugged areas. The average annual rainfall in highland and lowland areas ranges between 300 mm/yr and 200 mm/yr respectively [53].

Figure 3 illustrates groundwater levels and daily withdrawal rate. Geologically, Wadi Nu'man lies within the Makkah Quadrangle and is underlain by Cambrian plutonic rocks. The area also contains volcanic formations dating to the Tertiary period, along with clastic deposits associated with the Quaternary period. These sediments overlie the wadis and create favorable conditions for the formation of unconfined aquifers. The geological map of the study area is presented in Figure 4. It is noteworthy that these rock types can influence groundwater characteristics, as prolonged interaction between water and the surrounding rocks may gradually increase the salinity of the groundwater.

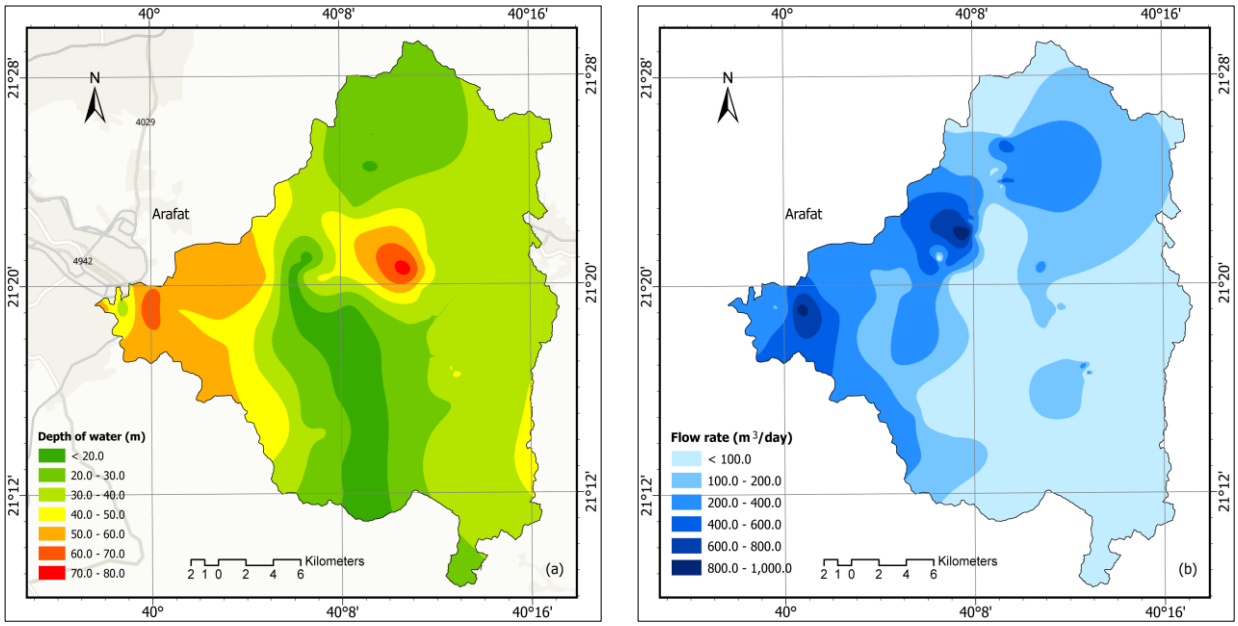

Figure 3. Hydrological information of Wadi Nu'man basin: (a) groundwater levels; (b) daily withdrawal rate

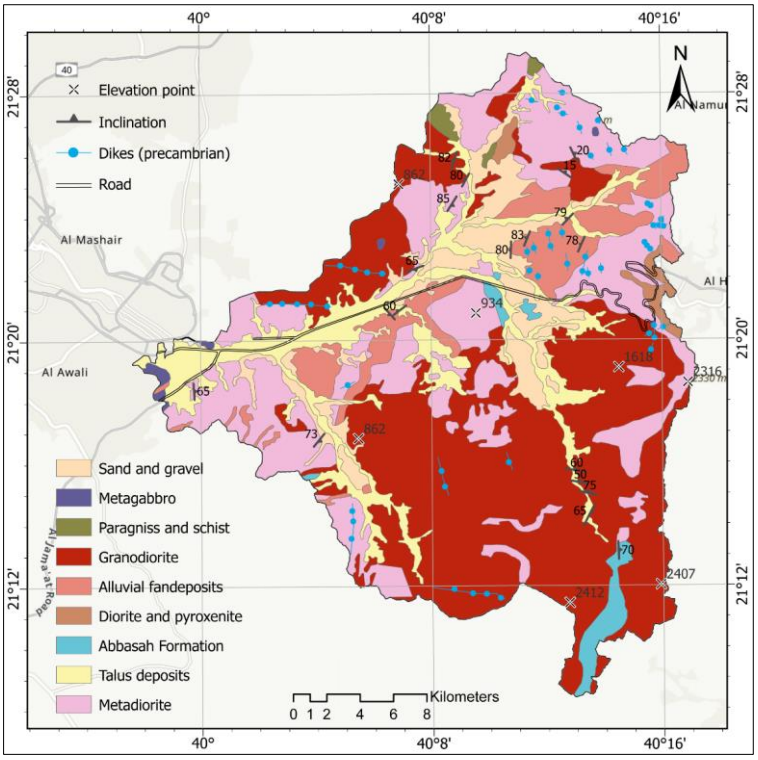

Figure 4. The geological map of Wadi Nu'man basin

The reasons behind the selection of Wadi Nu'man region for this study are: first, Wadi Nu'man represents one of the most groundwater-dependent basins in the Mecca, where groundwater supports both agricultural and domestic activities. Second, Wadi Nu'man area has experienced increasing urban expansion and intensive groundwater exploitation, which may contribute to land subsidence and surface deformation. Third, the availability of Sentinel-1 SAR data and groundwater observations, combined with the basin's geological and hydrological complexity, makes Wadi Nu'man a suitable case study for investigating groundwater–subsidence interactions using time-series InSAR analysis.

2.2. Research Data Collection

Data used in this research were collected from different sources including remote sensing imagery, field data and reports from ministry of water and electricity, Saudi Arabia. Regarding remote sensing data, this study utilizes the C-band SAR data from Sentinel-1 A, B satellites with approximately wavelength $\lambda = 5.6$ cm. These data are downloadable free of charge from the European Space Agency (ESA) [56, 57]. Dataset collection consists of five pairs of SAR images, Level1 interferometric Wide (IW) Single Look Complex (SLC) data, acquired from August 2015 until July 2025 as shown in Table 2. In addition to ALOS DEM model of a 12.5 m spatial resolution that was downloaded free from United States Geological Survey Site (USGS) site [58]. The selection of image pairs suitable for conducting interferograms were identified thanks to the Interferometry Baseline Tool Published by Alaska Satellite Facility (ASF), University of Alaska Fairbanks (UAF) [59].

Table 2. Detail information of Sentinel-1 images used

Type	Date	Mission	Track	Orbit	b_temp (days)	b_perp (m)	Coherence
Master	20 August 2016	Sentinel- 1A	14	12686	0	0	1
Slave	08 October 2017	Sentinel- 1B	14	7740	414	1	0.817
Master	25 May 2017	Sentinel- 1B	14	5815	0	0	1
Slave	30 July 2019	Sentinel- 1B	14	17365	792	0	0.768
Master	30 July 2019	Sentinel- 1B	14	17365	0	0	1
Slave	25 June 2021	Sentinel- 1B	14	27515	696	1	0.772
Master	07 July 2021	Sentinel- 1B	14	27690	0	0	1
Slave	08 August 2023	Sentinel- 1A	14	49786	762	8	0.758
Master	22 May 2024	Sentinel- 1A	14	53986	0	0	1
Slave	28 July 2025	Sentinel- 1C	14	2985	402	5	0.788

2.3. Interferometry and Interferogram formation

The raw data of radar imagery consists of two components which are: the phase information and the amplitude of the signal. When the aim is to find the change in the relief of a certain area, almost the phase is considered as the valuable source of information. Measuring the phase is considered as the primary step in the so-called interferometry Radar technique. The main concept lies in using radar images of different periods or from different orbits to detect any variation in altitude in the terrain. The distance between the two orbits in the plane perpendicular to the orbit is called the interferometer baseline where the perpendicular baseline (*Bn*) is the projection of the baseline perpendicular to the slant range as depicted in Figure 5. When relative positions of points on the ground surface slightly change in the time lag between the two SAR images, from orbit 1 and orbit 2, the interferometric phase *(*$\Delta\phi$*)*, can be calculated as Equation 1.

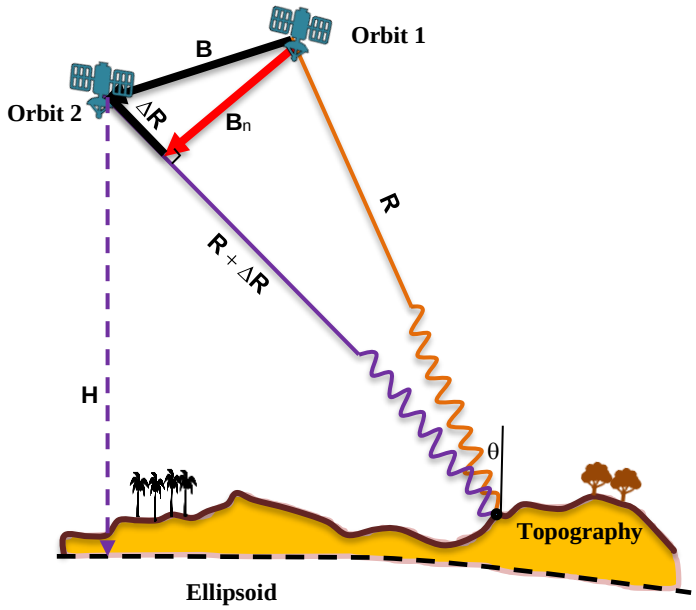

Figure 5. Differential SAR interferometry [55]

$$\Delta\phi = \frac{4\pi}{\lambda}(\Delta R) \quad (1)$$

where, ΔR represents the relative displacement on the slant range direction

The interferogram is generated by multiplying the complex values of the master image with the complex conjugate of a slave one. This process effectively averages the amplitudes of the corresponding pixels and computes the phase difference at each location. In InSAR applications, the perpendicular baseline plays a critical role. When the objective is to estimate terrain height, the altitude of ambiguity (ha) donates to the difference in height that produces a 2π phase shift after flattening of the interferogram is particularly important. It is inversely proportional to the perpendicular baseline as seen in Equation 2. As perpendicular baseline increases the sensitivity of the interferometric phase to topography increases, whereas a smaller perpendicular baseline enhances its sensitivity to surface deformation.

$$h_a = \frac{\lambda R sin\theta}{2B_n} \quad (2)$$

where, θ represents the incident angle, and B_n is the perpendicular baseline.

Differential interferometry allows for the measurement of centimeter-scale changes in elevation within a given terrain. The basic concept involves using images from different periods to detect any changes in elevation. Technically, this is achieved by subtracting two interferograms, one obtained before and one after the event that caused the three-dimensional change. After subtraction, the remaining fringes represent the magnitude of the elevation change experienced by the terrain. The interferometric phase (ϕ_{int}) is the sum of contributions from several factors, and the following equation can express this:

$$\phi_{int} = \phi_{displ} + \phi_{topo} + \phi_E + \phi_{atm} + \phi_{noise} \quad (3)$$

where, ϕ_{displ} represents the phase due to surface displacement, ϕ_{topo} refers to the phase caused by local topography, ϕ_E is the phase produced by a surface of constant elevation or orbital phase, ϕ_{atm} denotes the phase components due to the variation of atmospheric conditions, and ϕ_{noise} includes all the phase noise contributions that corrupt the interferometric SAR signal.

The principle of differential interferometric is to separate the topographic phase and displacement in an interferogram. The first one has to be completely removed to identify the displacement. The accuracy of surface displacement measurements greatly depends on the quality of the differential interferometric phase. Here, five deferential interferograms were generated to estimate the displacement happens during the time between the dates of those images.

2.4. Land Subsidence Estimation

The SAR data were processed using Sentinel Application Platform SNAP. It is an Eesa opensource software for scientific exploitation of earth observations. The interferometric processing chain consists of several key steps. The first step involves applying the orbit files to update the Sentinel-1 images with precise satellite position and velocity information, which becomes available a few days after acquisition. The second step is the co-registration of the two Sentinel-1 images, ensuring that each ground target aligns with the same pixel in both the master and slave images in range and azimuth. This process includes Back Geocoding and Enhanced Spectral Diversity, both of which help achieve precise co-registration. Then the next step is interferogram generation, followed by the De-burst operation to remove gaps between bursts. Multi looking is then applied to reduce speckles and improve image interpretability, where multi-looking factors of 4 looks in range and 1 look in azimuth were applied. To further reduce phase noise, a Goldstein phase filter is applied using a 32 × 32 window size and coherence threshold of 0.3. For phase unwrapping, the intermediate product is exported to the SNAPHU tool and then re-imported to SNAP for converting wrapped phase values into apparent displacement. Lastly, the step of terrain correction where the displacement map is corrected using the Range–Doppler Terrain Correction tool. The flowchart for the methodology applied is presented in Figure 6.

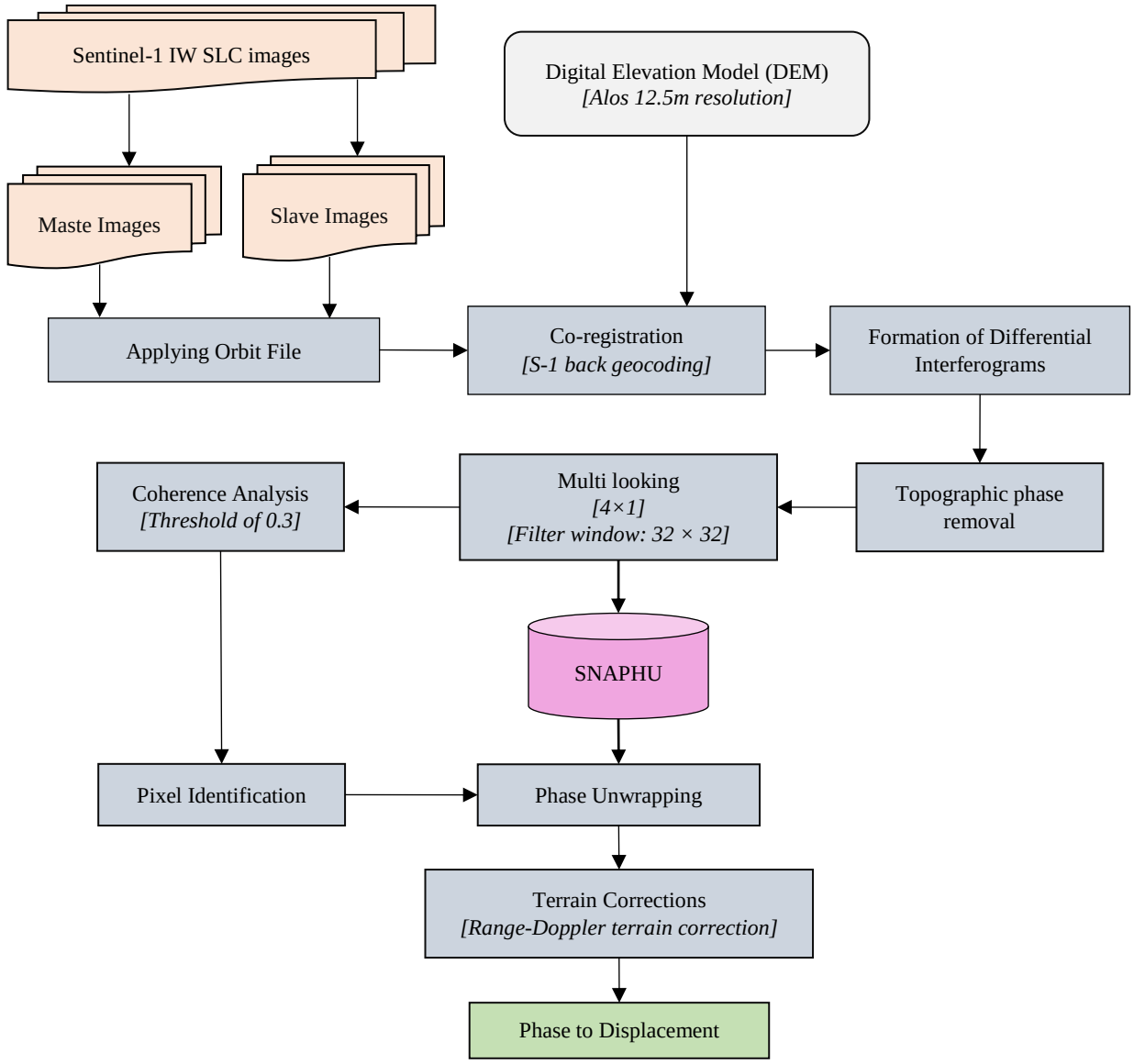

Figure 6. Flowchart for the methodology applied

2.5. Correlation Analysis

The relationship between the rate of flow, land subsidence, and the soil type were investigated in this study. Pearson correlation, one of the approaches broadly used to identify the relationships among variables, is used to quantify the temporal relationship between studied variables. The Pearson correlation coefficient (ρ) measures the correlation between two variables, *x* and *y*.

$$\rho_{xy} = \frac{\frac{\sum_{i=1}^{n} x_i y_i}{n} - \hat{x} \times \hat{y}}{\sigma_x \times \sigma_y} \quad (3)$$

where, n represents the number of observations. Mean value of x and y are represented by $\hat{x}$ and $\hat{y}$ respectively. Similarly, σ_x and σ_y represent the standard deviation of the two variables, x and y respectively. The coefficient r_{xy} ranges from -1 to +1. We utilized it to establish linear relations between rate of flow of groundwater from wells and the total land subsidence through the period of study.

3. Results

3.1. Land Deformation Monitoring

Starting from August 2016 and applying the methodology presented in section 2.4., cumulative subsidence of the study area was calculated for August 2016 to October 2017, May 2017 to July 2019, also from July 2019 to June 2021, then from July 2021 to August 2023, and finally from May 2024 to July 2025. Both the coherence and interferometric phase bands are included in the debursted interferograms. The difference in phase between the two images is pictured in the second band that appears to be as a spatially continuous image after the debursting process. Then the next step is the creation of the differential interferogram, in which the topographic phase is removed to isolate the deformation signal, as shown in the figure below. Figure 7-a illustrates the difference in the phase after eliminating the topographic component from the VV-polarized interferogram generated from the 2016 and 2017 image pair. The phase was then unwrapped using SNAPHU, producing a displacement map in centimeters along the line-of-sight (LOS). Finally, is the step of projecting the displacement via the terrain correction tool, as shown in Figure 7-b.

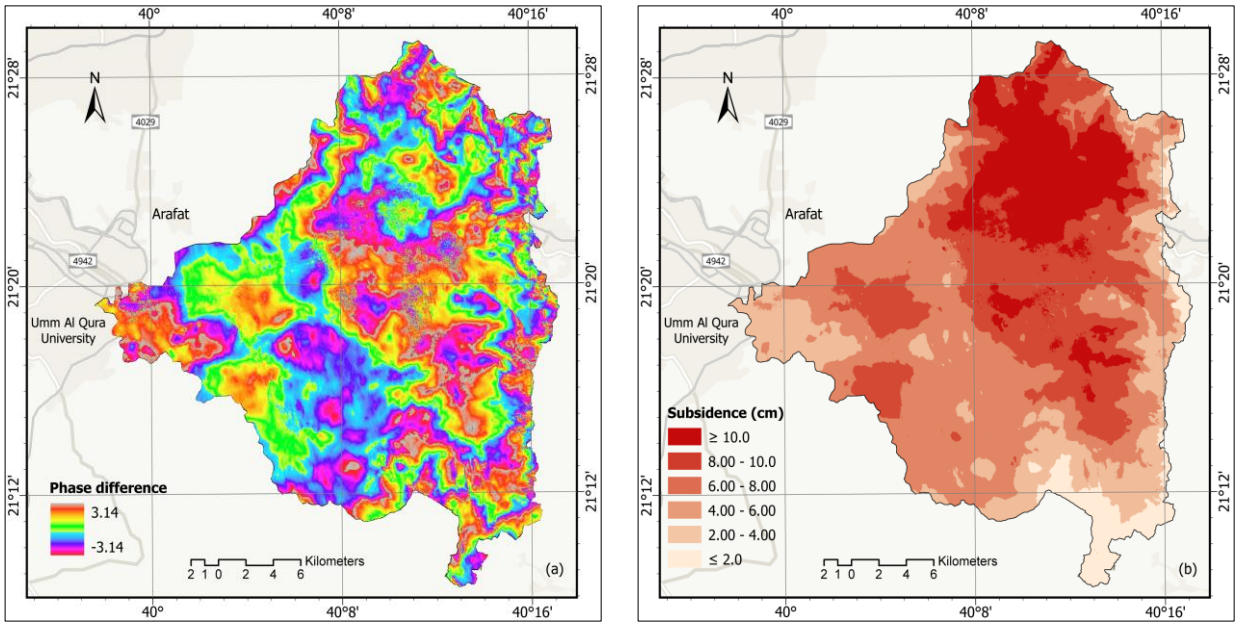

Figure 7. Land subsidence 2016 to 2017: (a) Phase difference after eliminating the topography from the VV-polarized interferogram; (b) Displacement in Wadi Nu'man basin 2016 to 2017

The displacements occurred in the study area during the different periods are depicted in Figure 8 whereas Table 3 summarizes the descriptive statistics of the land subsidence. The total subsidence of Wadi Nu'man basin (August 2016 –July 2025) estimated based on the proposed methodology is shown in Figure 9. It was noticed that the maximum value of subsidence reached 152.42 mm which indicates that there was a significant deformation occurring in the study area.

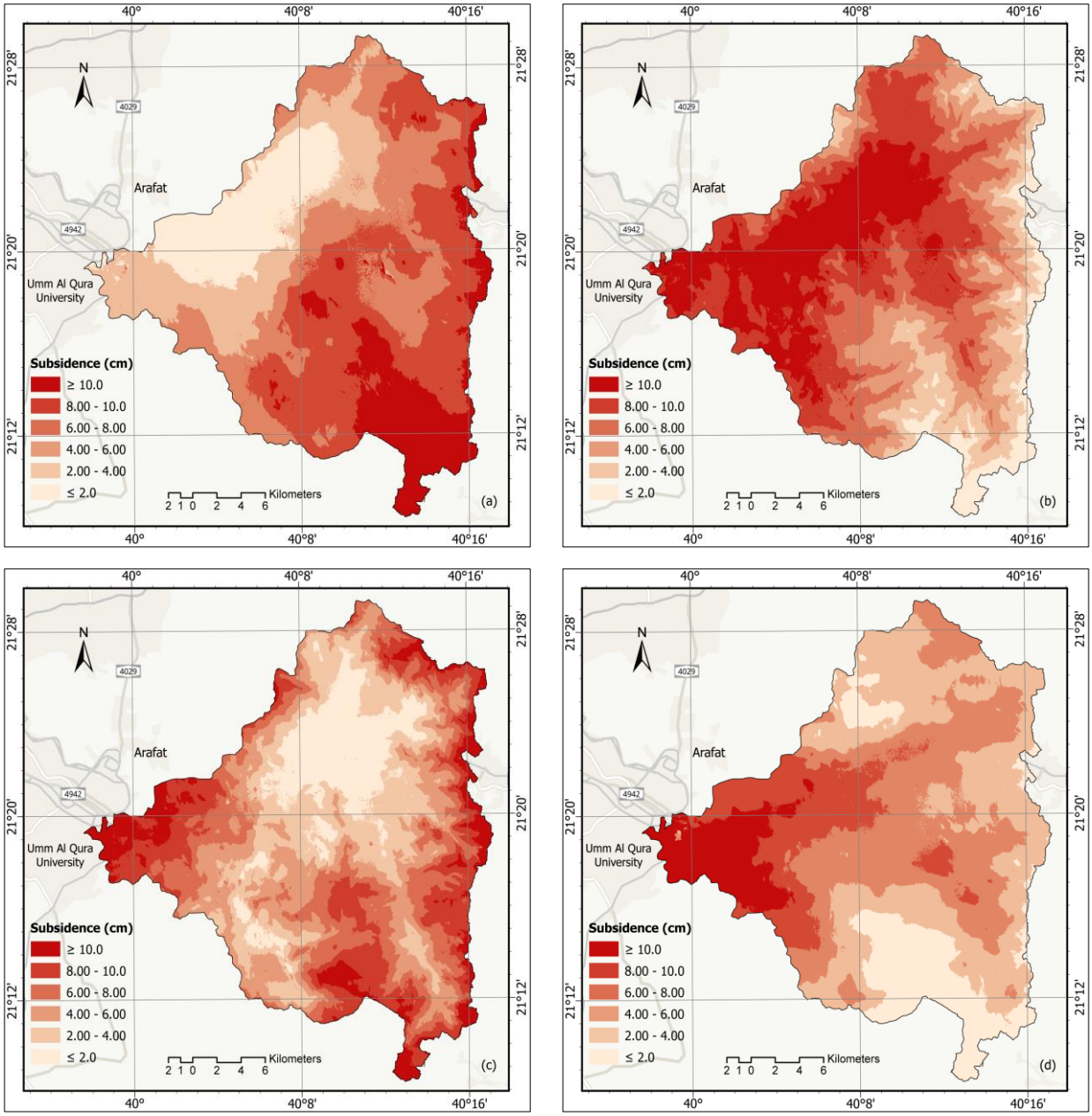

Figure 8. Displacement in Wadi Nu'man basin: (a) From May 2017 to July 2019; (b) From July 2019 to June 2021; (c) From July 2021 to August 2023; (d) From May 2024 to July 2025

Table 3. Descriptive statistics of land subsidence through the studied periods

Period	Minimum	Mean	Maximum	S.D	Median	Skewness	Kurtosis	NMAD
2015-2017	0.001	3.029	7.093	1.345	2.897	0.246	-0.431	1.385
2017-2019	0.002	1.743	4.469	0.834	1.828	-0.142	-0.626	0.836
2019-2021	0.000	3.700	9.194	1.784	4.012	-0.316	-0.788	1.905
2021-2023	0.000	1.637	7.152	1.217	1.431	1.023	1.104	1.182
2023-2025	0.000	1.806	5.165	0.834	1.814	0.137	-0.084	0.785
2015-2025	0.003	5.846	15.242	1.752	6.031	-0.308	0.641	1.617

The descriptive statistics provide deeper insight into temporal fluctuations in the deformation, the standard deviation value ranges between 0.834 to 1.784 that reflects a spatial heterogeneity in subsidence behavior. The maximum recorded displacement reached 91.94 mm (2019-2021) with mean value of 37.0 mm; this makes this period have the highest deformation. The subsidence distribution alternates between being right- and left-skewed across the years, Kurtosis values close to zero suggest that most distributions are relatively balanced spread of deformation values, and Normalized Median Absolute Deviation (NMAD) values confirm that the results are statistically consistent.

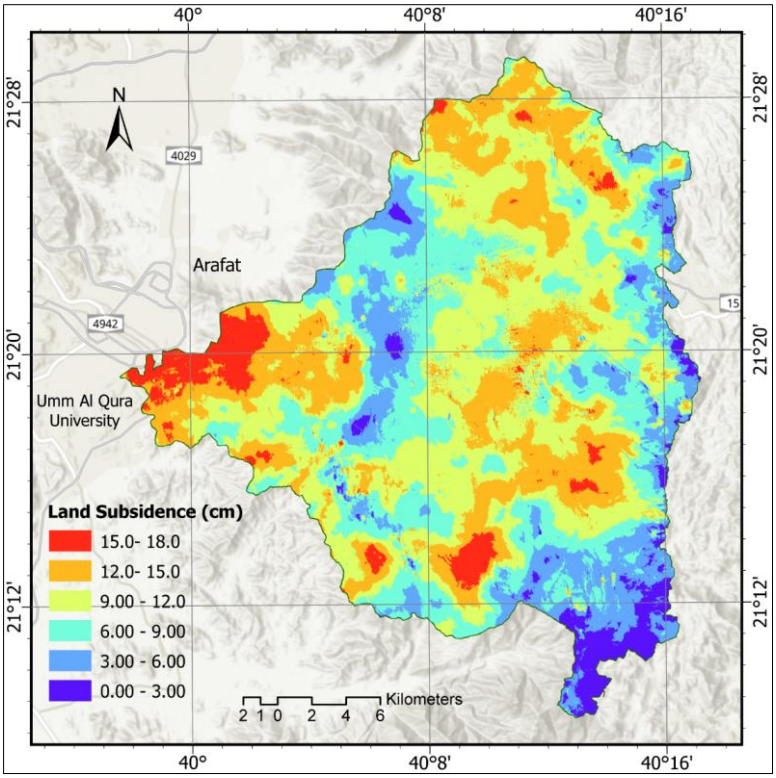

Figure 9. The cumulative land subsidence of Wadi Nu'man basin (August 2016 –July 2025)

Figure 9 demonstrates progressive land subsidence over nearly a decade, with certain zones exhibiting significantly greater displacement, especially in low-lying areas. The violin plot in Figure 10 illustrates the distribution and density of subsidence values across the different time intervals. The figure clearly shows a consistent central clustering of deformation values in all intervals, along with wider tails in some periods, indicating localized pockets of extreme subsidence. Additionally, the presence of multimodal patterns in certain intervals reflects the spatial variability of vertical deformation within the study area.

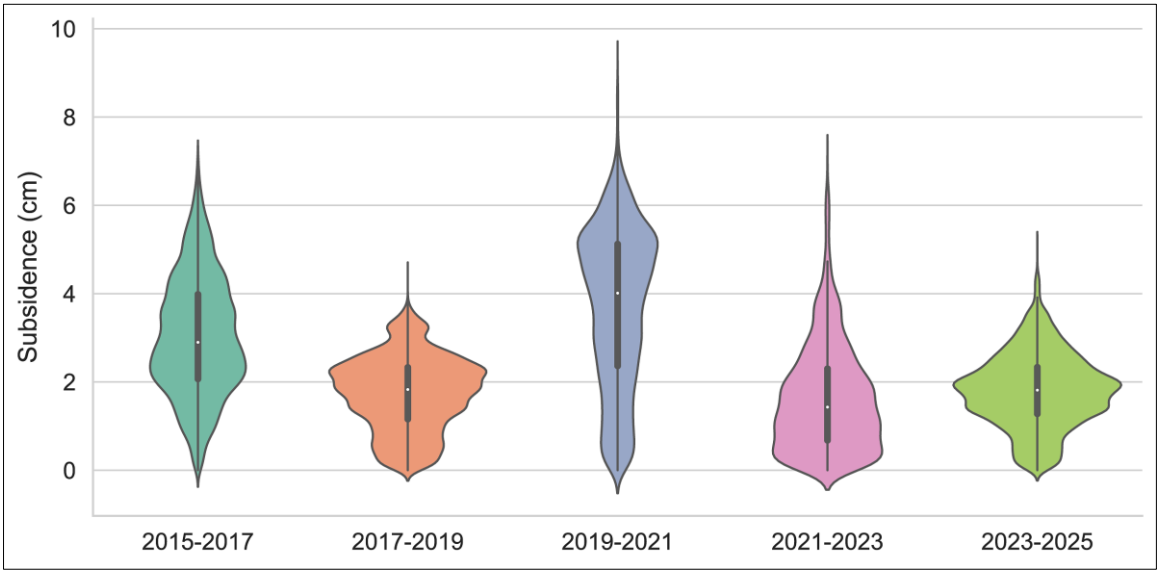

Figure 10. Violin plot for land subsidence of Wadi Nu'man basin for different periods

3.2. Subsidence Inducing Factors

3.2.1. Correlation with the Rate of Groundwater Flow

This part examines the rate of flow of groundwater and the vertical land subsidence correlation. Based on the results, the box plot depicted in Figure 11 relating groundwater flow rate to surface deformation points to a clear relationship between higher extraction rates and increased subsidence. As the rate of flow increases, the median

subsidence elevates with an enlargement in interquartile ranges, and the tendency of boxplot to be right skewed increases. Also, no extreme outliers observed. This pattern suggests that groundwater pumping is a key driver of deformation.

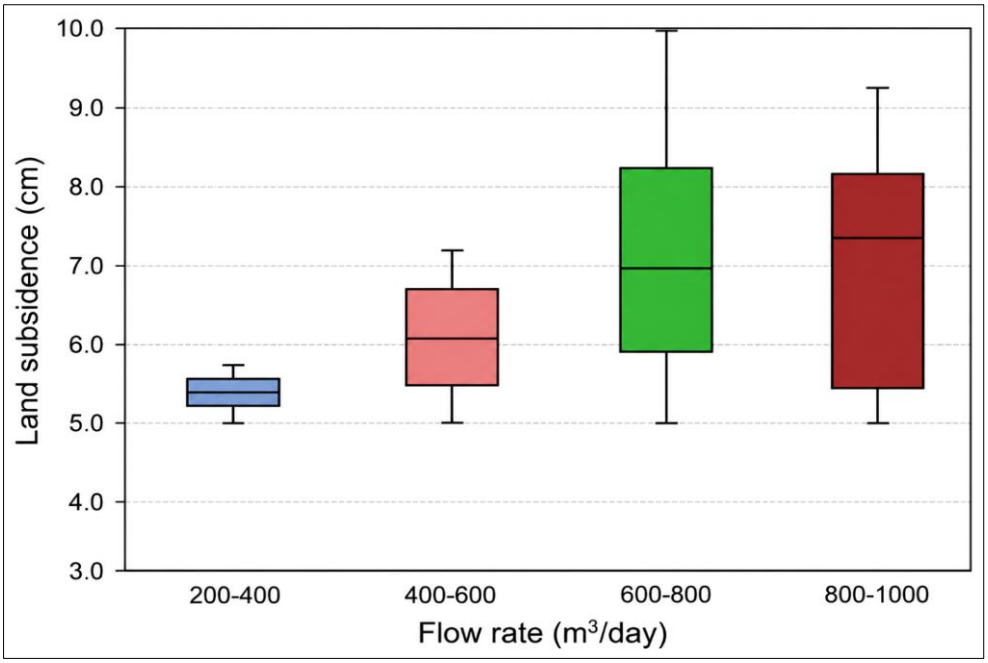

Figure 11. Boxplot for land subsidence of Wadi Nu'man basin with the groundwater discharge rate

3.2.2. The effect of Type of Soil on Surface Deformation

To analyze the correlation between soil classification and land subsidence, Figure 12 presents boxplots for land subsidence of the Wadi Nu'man basin with different soil types. The figure indicates that subsidence behavior varies considerably between soil classes. Talus deposits and Metagabbro tend to exhibit higher median subsidence with larger variability. This supports that deposits with fine-grained stratigraphy play an important role in controlling deformation response. The interaction plot in Figure 13 reveals that the strongest subsidence occurs in areas where high groundwater extraction overlaps with compressible soil types like Talus deposits, Metadiorite and Metagabbro. However, subsidence is not solely a function of groundwater pumping; it is also influenced by the properties of the soil itself. Inside the studied area, only the Abbasah Formation and the diorite–pyroxenite units showed a significant correlation between vertical subsidence and groundwater flow rates ($R^2 = 0.67$).

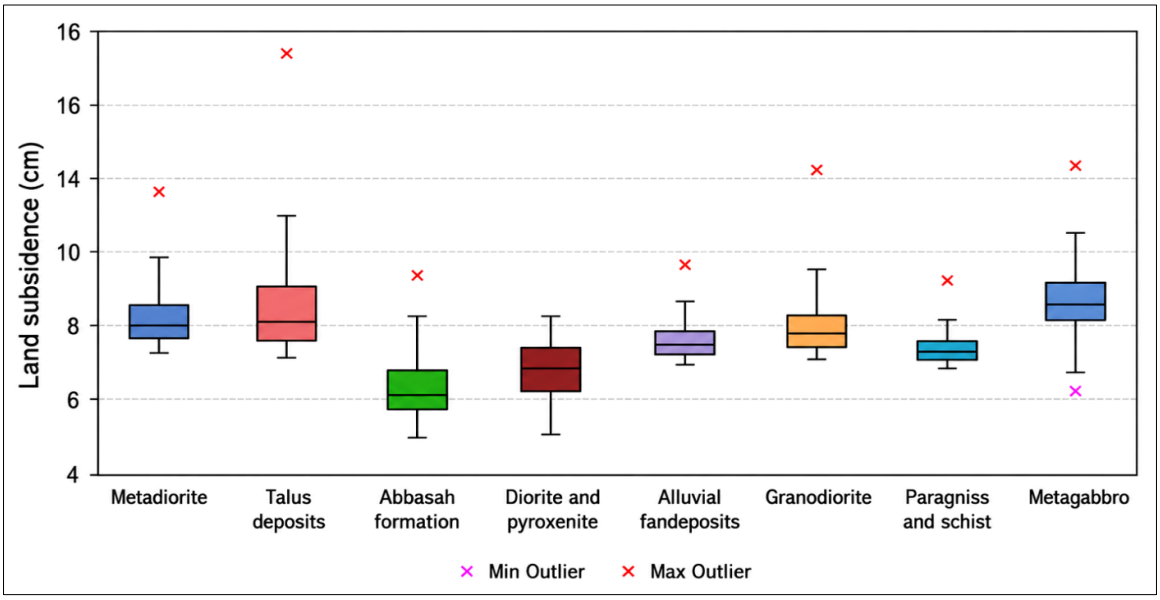

Figure 12. Boxplot for land subsidence of Wadi Nu'man basin with different soil types

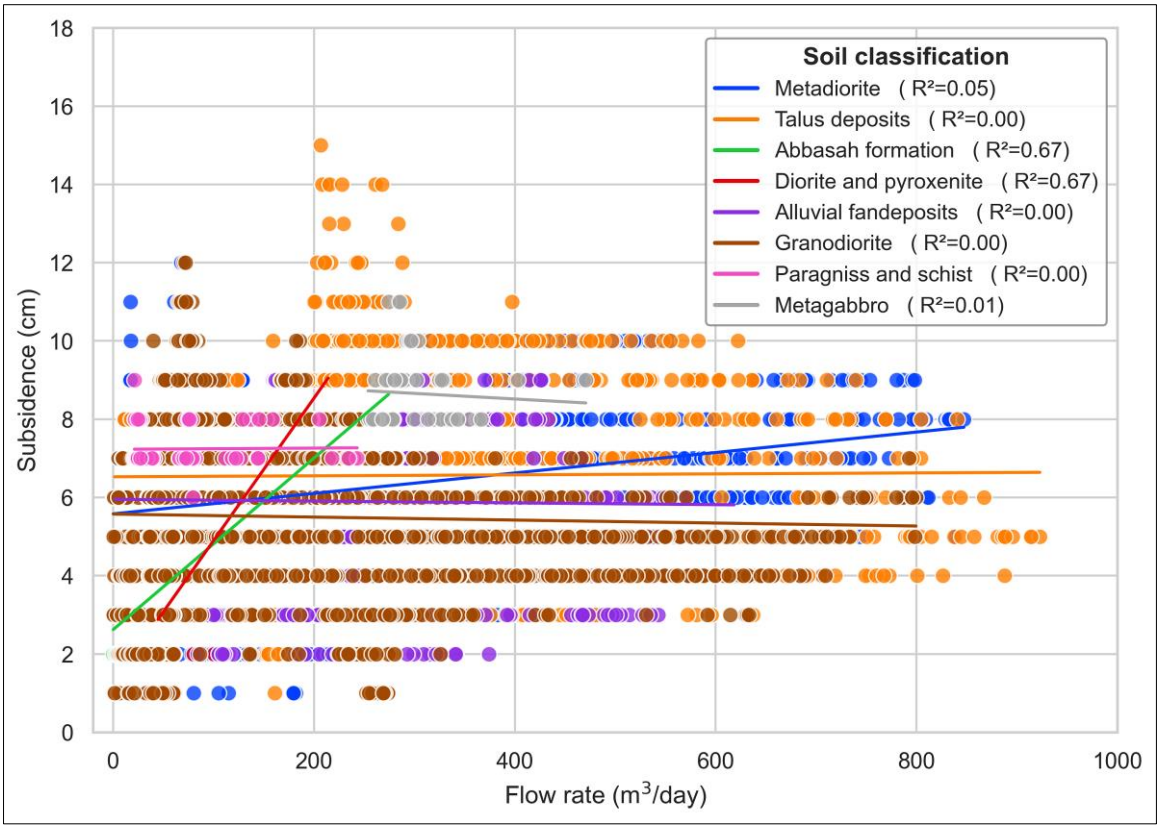

Figure 13. Correlation of land subsidence of Wadi Nu'man with flow rate on different soil types

4. Discussion

This study integrated the synthetic aperture radar (SAR) imagery and the data gathered about flow rates, the water table depth and the geological information in Wadi Nu'man, Saudi Arabia to accurately observe the land subsidence and analyze the deformation occurred in Wadi Nu'man through the period (2016-2025). In this research a collection of Sentinel-1A, Sentinel-1B, and Sentinel-1C imagery was utilized to enable extended temporal monitoring of surface deformation which may result in potential inconsistencies between sensors. Insignificant variations in temporal coherence and interferometric measurements may arise due to differences in orbital configuration, radiation behavior, sensor calibration, and temporal resolution. Furthermore, the data of Sentinel-1B was not available after 2021which affected the continuity of data within the time series. To minimize these effects, all imagery datasets were processed using consistent workflow, including accurate orbit correction, co-registration enhancement, radiometric calibration, and standardized interferometric processing parameters. Additionally, the use of the same acquisition mode and orbit direction helped maintain temporal consistency throughout the analysis.

The time series InSAR results clearly explored the multiple subsidence and demonstrated the spatiotemporal evaluation of surface deformation. Land subsidence is unevenly distributed, where high values correspond to urban areas with heavy water consumption and agricultural regions of intensive irrigation. This highlights hydraulic stress being the dominant factor of land subsidence occurred in the region. The biggest cumulative subsidence is observed in the southern and Western parts of the study area where a heavy withdrawal of water exists. That overexploitation of groundwater, for a long time, leads to a decline in the hydraulic head and increase in soil consolidation. These results are compatible with the findings in Yu et al. [40] and Li et al. [41].

During the study period, a significant subsidence was observed at average rates of < 4 cm/year, with maximum values exceed 15.2 cm in some places. By examining groundwater depths in the study area and their relationship to total subsidence, we find notable variations in groundwater depth, as shown in Figure 3a. This variation is attributed to differences in land elevations and slopes. In mountainous areas with steep gradients, groundwater tends to lie deeper, whereas in low-lying areas the water table is much shallower. These low areas also contain most of the groundwater wells, where extraction rates are higher, such as in the Wadi Zubaydah basin and Wadi Arar, where the average groundwater depths are 18.79 m and 18.6 m, respectively. The average daily extraction in these areas reached 202.44 and 123.37 m³/day, respectively. Also, notably the similarity between the intensity map of groundwater exploitation presented in Figure 3b with the distribution of subsidence map presented in Figure 9. This pattern corresponds well with the distribution of cumulative subsidence during the studying interval, as displayed in Figure 9, where the vertical deformation exceeded 15 cm in these zones.

The influence of soil type highlights the geotechnical dimension of the problem. Areas underlain by Quaternary or alluvial deposits—known for their high compressibility—exhibit more pronounced deformation [3, 46, 60]. This aligns with theoretical expectations that fine-grained or clay-rich materials undergo greater compaction when pore pressure decreases. By examining the relationship between the observed subsidence and soil type under different groundwater extraction rates, it is evident that no correlation exists for most soil types, except for soils (Abbasah Formation and the diorite–pyroxenite). This is attributed to the mechanical properties of these soils and proves a degree of consistency with the results obtained in Kan et al. [61]. As obvious in Figure 12, these two soils have the lowest value of land subsidence for about 9 years, the study time lag. This is evidence on that deformation is due to transient responses synchronous with groundwater and it does not represent a residual deformation from historical groundwater variations [54].

The stronger correlation noticed within the Abbasah Formation and the diorite–pyroxenite units may be attributed to the geological and hydrogeological characteristics of these formations. In fact, these types of formations are characterized by weathered materials and fractures that may facilitate the groundwater to be stored inside. They are more sensitive to compaction and water extraction or ground water level fluctuations. Therefore, groundwater withdrawal, even at a small rate, throughout these formations may cause a significant surface deformation that can be measured through InSAR analysis. On the other hand, the weaker correlations observed in other geological units may be related to the solidness, lower porosity, and compressibility of these formations, which makes them independent of the water level fluctuation and groundwater abstraction intensity. These findings indicate that the relationship between groundwater dynamics and land subsidence is strongly controlled by local geological and hydrogeological conditions.

Some limitations and potential enhancements in future studies arise in this study. First, this study is based on the assumption that land subsidence occurs only as a result of changes in effective stresses caused by overextraction of groundwater, lacking consideration of the effect of tectonic activity and groundwater level variations. Second, the investigation in this study was constrained by data limitations. On one hand, reliance on C-band Sentinel-1 imagery restricted the temporal continuity of long-term monitoring; on the other hand, the available groundwater-depth data was limited. Future work will focus on field monitoring to enhance and validate deformation detection, in addition to using numerical models to simulate the interaction of ground water extraction and land deformation.

5. Conclusion

In this paper, land subsidence in the Wadi Nu'man Basin, Saudi Arabia, was investigated using a set of C-band SAR images acquired from the Sentinel-1A and Sentinel-1B satellites. By applying the proposed methodology, time-series maps of surface deformation, together with the magnitude and spatial distribution of long-term subsidence from 2016 to 2025, were generated. The results indicate that the study area is subjected to an average deformation velocity of less than 4 cm/year, while the maximum recorded subsidence reached 15.2 cm in the most compressible soils.

Based on the analysis, land subsidence was found to increase with rising groundwater extraction rates. However, only two soil units, namely the Abbasah Formation and the diorite–pyroxenite unit, exhibited a significant positive correlation between subsidence and groundwater flow rate. This study demonstrates that InSAR-based monitoring is a valuable tool for identifying deformation patterns in the Wadi Nu'man Basin. It also provides important support for risk assessment, particularly given that Wadi Nu'man lies within the expansion corridor of Mecca, where consideration of land subsidence risks in urban planning and infrastructure development is essential.

Therefore, addressing the challenges associated with sustainable groundwater management and regulating groundwater extraction are of critical importance. This can be achieved through the identification of crop types, cultivated areas, and irrigation methods. In addition, various management strategies should be adopted, including the implementation of total withdrawal controls and dynamic quota systems aligned with crop growth cycles. Furthermore, integrating geological and hydrological datasets will enhance the modeling and understanding of aquifer behavior.

This study was constrained by several data-related limitations. Groundwater depth records were sparse and insufficient in both spatial and temporal coverage. In addition, reliance on C-band Sentinel-1 imagery limited the continuity of long-term deformation monitoring.

6. Declarations

6.1. Data Availability Statement

The data presented in this study are available on request from the corresponding author.

6.2. Funding

This project was funded by the Deanship of Scientific Research (DSR) at King Abdulaziz University, Jeddah, under grant no. IPP: 1041-137-2025. The author, therefore, acknowledge with thanks DSR for technical and financial support.

6.3. Acknowledgments

The author gratefully acknowledges the technical and financial support provided by the Ministry of Education and King Abdulaziz University, DSR, Jeddah, Saudi Arabia. Also, the author is grateful to Engineer Reem Yehia for helping in preparing data.

6.4. Conflicts of Interest

The author declares no conflict of interest.

7. References

[1] Rohde, M. M., Stella, J. C., Roberts, D. A., & Singer, M. B. (2021). Groundwater dependence of riparian woodlands and the disrupting effect of anthropogenically altered streamflow. Proceedings of the National Academy of Sciences of the United States of America, 118(25). doi:10.1073/pnas.2026453118.

[2] Chen, Y., Liao, M., Wu, J., Li, X., Xiong, F., Liu, S., Feng, Y., & Wang, X. (2022). Elastic and Inelastic Ground Deformation in Shanghai Lingang Area Revealed by Sentinel-1, Leveling, and Groundwater Level Data. Remote Sensing, 14(11), 2693. doi:10.3390/rs14112693.

[3] Wang, R., Luo, Y., Yang, Y., Tian, F., Zhou, Y., & Tian, M. Z. (2015). Characterization of land subsidence induced by groundwater withdrawals in Wenyu River alluvial fan, Beijing, China. Proceedings of the International Association of Hydrological Sciences, 372, 481–484. doi:10.5194/piahs-372-481-2015.

[4] Lu, Y. Y., Ke, C. Q., Jiang, H. J., & Chen, D. L. (2019). Monitoring urban land surface deformation (2004–2010) from InSAR, groundwater and levelling data: A case study of Changzhou city, China. Journal of Earth System Science, 128(6), 159. doi:10.1007/s12040-019-1173-y.

[5] Galloway, D. L., & Burbey, T. J. (2011). Review: Regional land subsidence accompanying groundwater extraction. Hydrogeology Journal, 19(8), 1459–1486. doi:10.1007/s10040-011-0775-5.

[6] Cigna, F., Ramírez, R. E., & Tapete, D. (2021). Accuracy of sentinel-1 PSI and SBAS InSAR displacement velocities against GNSS and geodetic leveling monitoring data. Remote Sensing, 13(23), 4800. doi:10.3390/rs13234800.

[7] Van Ty, T., Thu Minh, H. V., Avtar, R., Kumar, P., Van Hiep, H., & Kurasaki, M. (2021). Spatiotemporal variations in groundwater levels and the impact on land subsidence in CanTho, Vietnam. Groundwater for Sustainable Development, 15, 100680. doi:10.1016/j.gsd.2021.100680.

[8] Gezgin, C. (2022). The influence of groundwater levels on land subsidence in Karaman (Turkey) using the PS-InSAR technique. Advances in Space Research, 70(11), 3568–3581. doi:10.1016/j.asr.2022.08.003.

[9] Metwaly, M., Elawadi, E., Taha, A. I., El-Qady, G., Anter, A., & Szalai, S. (2021). Geophysical studies for the aquifer properties along Wadi Nu'man, Holy Makkah area, Saudi Arabia. Arabian Journal of Geosciences, 14(22), 2316. doi:10.1007/s12517-021-08661-4.

[10] Sharaf, M. A. M. (2013). Trace Elements Hydrochemistry and Suitability of the Groundwater in Wadi An Numan Area, Makkaah District, Western Arabian Shield, Saudi Arabia. Arabian Journal for Science and Engineering, 38(7), 1871–1887. doi:10.1007/s13369-012-0399-7.

[11] Abdelkarim, A., & Gaber, A. F. D. (2019). Flood risk assessment of the Wadi Nu'man basin, Mecca, Saudi Arabia (during the period, 1988-2019) based on the integration of geomatics and hydraulic modeling: A case study. Water (Switzerland), 11(9), 1887. doi:10.3390/w11091887.

[12] Şen, Z., As-Sefry, S., & Al-Harithy, S. (2017). Strategic management of groundwater resources in the Arabian Peninsula: Wadi Na'man case. Arabian Journal of Geosciences, 10(3), 50. doi:10.1007/s12517-016-2824-9.

[13] Zhang, L., Lu, Z., Ding, X., Jung, H. S., Feng, G., & Lee, C. W. (2012). Mapping ground surface deformation using temporarily coherent point SAR interferometry: Application to Los Angeles Basin. Remote Sensing of Environment, 117, 429–439. doi:10.1016/j.rse.2011.10.020.

[14] Perissin, D., & Wang, T. (2012). Repeat-pass SAR interferometry with partially coherent targets. IEEE Transactions on Geoscience and Remote Sensing, 50(1), 271–280. doi:10.1109/TGRS.2011.2160644.

[15] Guo, L., Gong, H., Zhu, F., Zhu, L., Zhang, Z., Zhou, C., Gao, M., & Sun, Y. (2019). Analysis of the spatiotemporal variation in land subsidence on the Beijing Plain, China. Remote Sensing, 11(10), 1170. doi:10.3390/rs11101170.

[16] Shi, W., Chen, G., Meng, X., Jiang, W., Chong, Y., Zhang, Y., Dong, Y., & Zhang, M. (2020). Spatial-temporal evolution of land subsidence and rebound over Xi'an in western China revealed by SBAS-InSAR analysis. Remote Sensing, 12(22), 3756. doi:10.3390/rs12223756.

[17] Rajaoalison, H., & Knez, D. (2021). Current trends in land subsidence of the North-Central part of Poland using DInSAR technique. E3S Web of Conferences, 266, 3006. doi:10.1051/e3sconf/202126603006.

[18] Zhang, R., Wang, T., Liu, G., Shama, A., Liu, A., Wang, X., Deng, L., & Mao, W. (2025). Ground subsidence evolution and groundwater variation in the middle route of south to north water diversion project. Scientific Reports, 15(1), 19220. doi:10.1038/s41598-025-04307-7.

[19] Rogers, A. E. E., & Ingalls, R. P. (1969). Venus: Mapping the surface reflectivity by radar interferometry. Science, 165(3895), 797–799. doi:10.1126/science.165.3895.797.

[20] Yixian, T., Hong, Z., & Chao, W. (2007). Long term monitoring of urban subsidence by Permanent Scatterer DInSAR. Progress in Natural Science, 17(1), 107-111. doi:10.1080/10020070612331343233.

[21] Greif, V., & Vlcko, J. (2012). Monitoring of post-failure landslide deformation by the PS-InSAR technique at Lubietova in Central Slovakia. Environmental Earth Sciences, 66(6), 1585–1595. doi:10.1007/s12665-011-0951-x.

[22] Bianchini, S., Ciampalini, A., Raspini, F., Bardi, F., Di Traglia, F., Moretti, S., & Casagli, N. (2015). Multi-Temporal Evaluation of Landslide Movements and Impacts on Buildings in San Fratello (Italy) By Means of C-Band and X-Band PSI Data. Pure and Applied Geophysics, 172(11), 3043–3065. doi:10.1007/s00024-014-0839-2.

[23] Simons, M., Fialko, Y., & Rivera, L. (2002). Coseismic deformation from the 1999 Mw 7.1 Hector Mine, California, earthquake as inferred from InSAR and GPS observations. Bulletin of the Seismological Society of America, 92(4), 1390–1402. doi:10.1785/0120000933.

[24] Ferretti, A., Prati, C., & Rocca, F. (2001). Permanent scatterers in SAR interferometry. IEEE Transactions on Geoscience and Remote Sensing, 39(1), 8–20. doi:10.1109/36.898661.

[25] Berardino, P., Fornaro, G., Lanari, R., & Sansosti, E. (2002). A new algorithm for surface deformation monitoring based on small baseline differential SAR interferograms. IEEE Transactions on Geoscience and Remote Sensing, 40(11), 2375–2383. doi:10.1109/TGRS.2002.803792.

[26] Khan, R., Li, H., Afzal, Z., Basir, M., Arif, M., & Hassan, W. (2021). Monitoring subsidence in urban area by PSInSAR: A case study of Abbottabad city, northern Pakistan. Remote Sensing, 13(9), 1651. doi:10.3390/rs13091651.

[27] Li, S., Xu, W., & Li, Z. (2022). Review of the SBAS InSAR Time-series algorithms, applications, and challenges. Geodesy and Geodynamics, 13(2), 114–126. doi:10.1016/j.geog.2021.09.007.

[28] Wang, T., Zhang, R., Zhan, R., Shama, A., Liao, M., Bao, X., He, L., & Zhan, J. (2022). Subsidence Monitoring and Mechanism Analysis of Anju Airport in Suining Based on InSAR and Numerical Simulation. Remote Sensing, 14(15), 3759. doi:10.3390/rs14153759.

[29] Inglada, J., & Adragna, F. (2002). Blind source separation applied to multitemporal series of differential SAR interferograms. International Geoscience and Remote Sensing Symposium (IGARSS), 2, 1240–1242. doi:10.1109/igarss.2002.1025901.

[30] Ballatore, P. (2006). Synthetic aperture radar interferometry: Separation of atmospheric artifacts from effects due to the topography and the terrain displacements. Earth, Planets and Space, 58(8), 927–935. doi:10.1186/BF03352597.

[31] Elhag, M., Chaabani, A., & Zhang, L. (2025). Assessment of surface deformation patterns using InSAR data: Implications for human impacts in Makkah City, Saudi Arabia. Kuwait Journal of Science, 52(3), 100419. doi:10.1016/j.kjs.2025.100419.

[32] Wang, S., Chen, Y., Ding, K., Gao, Y., Tan, K., & Du, P. (2025). MCR-PFNet: A novel InSAR interferometric phase filtering method for complex noise and large gradient deformations. International Journal of Applied Earth Observation and Geoinformation, 140, 104621. doi:10.1016/j.jag.2025.104621.

[33] Hamid, M. S., Ghetas, M., Reda, K. M., & Safy, M. (2026). Optimal feature-based InSAR phase filtering framework using convolutional neural network and mathematical morphology. Egyptian Journal of Remote Sensing and Space Science, 29(1), 28–43. doi:10.1016/j.ejrs.2026.01.001.

[34] Chen, M., Tomás, R., Li, Z., Motagh, M., Li, T., Hu, L., Gong, H., Li, X., Yu, J., & Gong, X. (2016). Imaging land subsidence induced by groundwater extraction in Beijing (China) using satellite radar interferometry. Remote Sensing, 8(6), 468. doi:10.3390/rs8060468.

[35] Si, Y., Chen, B., Gong, H., & Gao, M. (2018). Temporal and Spatial Evolution of Land Subsidence Induced by Groundwater Exploitation and Construction in the Eastern Chaoyang District, Beijing, China. Journal of the Indian Society of Remote Sensing, 46(10), 1657–1665. doi:10.1007/s12524-018-0821-z.

[36] Ceccatelli, M., Del Soldato, M., Solari, L., Fanti, R., Mannori, G., & Castelli, F. (2021). Numerical modelling of land subsidence related to groundwater withdrawal in the Firenze-Prato-Pistoia basin (central Italy). Hydrogeology Journal, 29(2), 629–649. doi:10.1007/s10040-020-02255-2.

[37] Peng, M., Lu, Z., Zhao, C., Motagh, M., Bai, L., Conway, B. D., & Chen, H. (2022). Mapping land subsidence and aquifer system properties of the Willcox Basin, Arizona, from InSAR observations and independent component analysis. Remote Sensing of Environment, 271, 112894. doi:10.1016/j.rse.2022.112894.

[38] Wang, Z., Liu, Y., Zhang, Y., Liu, Y., Wang, B., & Zhang, G. (2022). Spatially Varying Relationships between Land Subsidence and Urbanization: A Case Study in Wuhan, China. Remote Sensing, 14(2), 291. doi:10.3390/rs14020291.

[39] Li, C., Wang, Y., Yu, J., Gong, H., Li, X., Yang, X., Cheng, H., Li, X., & Shao, K. (2025). Estimation of inelastic skeletal storativity based on SAR-derived land subsidence and groundwater variation in Beijing Plain, China. Journal of Hydrology: Regional Studies, 57, 102161. doi:10.1016/j.ejrh.2024.102161.

[40] Yu, Z., Wang, Q., Gong, H., Zhou, C., Chen, B., & Wang, Y. (2025). Multi-Scale Time Series InSAR Integrated with ICA for Deciphering the Coupling Mechanism Between Groundwater Dynamics and Surface Deformation. Land, 14(5), 971. doi:10.3390/land14050971.

[41] Li, M., Ge, D., Guo, X., Zhang, L., Liu, B., Wang, Y., Wu, Q., Wan, X., & Wang, Y. (2023). Mapping and Analyses of Land Subsidence in Hengshui, China, Based on InSAR Observations. Land, 12(9), 1684. doi:10.3390/land12091684.

[42] Zhang, Y., Liu, S., Lan, K., Wu, L., Han, Y., Liu, Y., & Yu, B. X. (2026). Land subsidence in urban lake-infilled areas detected by Radarsat-2 InSAR time-series: The case of Shahu and Nanhu Lake in Wuhan, China. Journal of Hydrology, 672, 135408. doi:10.1016/j.jhydrol.2026.135408.

[43] Daud, N., Dasho, O., & Shirzaei, M. (2026). Probabilistic modeling of InSAR-derived land subsidence hazard in New York City for transportation infrastructure damage risk assessments. International Journal of Applied Earth Observation and Geoinformation, 146, 105118. doi:10.1016/j.jag.2026.105118.

[44] Chaussard, E., Milillo, P., Bürgmann, R., Perissin, D., Fielding, E. J., & Baker, B. (2017). Remote Sensing of Ground Deformation for Monitoring Groundwater Management Practices: Application to the Santa Clara Valley during the 2012–2015 California Drought. Journal of Geophysical Research: Solid Earth, 122(10), 8566–8582. doi:10.1002/2017JB014676.

[45] Awasthi, S., Jain, K., Bhattacharjee, S., Gupta, V., Varade, D., Singh, H., Narayan, A. B., & Budillon, A. (2022). Analyzing urbanization induced groundwater stress and land deformation using time-series Sentinel-1 datasets applying PSInSAR approach. Science of the Total Environment, 844, 157103. doi:10.1016/j.scitotenv.2022.157103.

[46] Yu, H., Gong, H., Chen, B., Liu, K., & Gao, M. (2020). Analysis of the influence of groundwater on land subsidence in Beijing based on the geographical weighted regression (GWR) model. Science of the Total Environment, 738, 139405. doi:10.1016/j.scitotenv.2020.139405.

[47] Castellazzi, P., & Schmid, W. (2021). Interpreting C-band InSAR ground deformation data for large-scale groundwater management in Australia. Journal of Hydrology: Regional Studies, 34, 100774. doi:10.1016/j.ejrh.2021.100774.

[48] Razeghi, M., Tregoning, P., Shirzaei, M., Ghobadi-Far, K., McClusky, S., & Renzullo, L. (2022). Characterization of Changes in Groundwater Storage in the Lachlan Catchment, Australia, Derived From Observations of Surface Deformation and Groundwater Level Data. Journal of Geophysical Research: Solid Earth, 127(12). doi:10.1029/2022JB024669.

[49] Zhao, Y., Wang, C. L., & Bi, J. (2020). Analysis of Fractured Rock Permeability Evolution under Unloading Conditions by the Model of Elastoplastic Contact between Rough Surfaces. Rock Mechanics and Rock Engineering, 53(12), 5795–5808. doi:10.1007/s00603-020-02224-x.

[50] Chen, B., Gong, H., Chen, Y., Li, X., Zhou, C., Lei, K., Zhu, L., Duan, L., & Zhao, X. (2020). Land subsidence and its relation with groundwater aquifers in Beijing Plain of China. Science of the Total Environment, 735, 139111. doi:10.1016/j.scitotenv.2020.139111.

[51] Aggarwal, A., Srivastava, P. K., Gupta, D. K., & Chatterjee, R. S. (2021). Estimating regional land subsidence in Mehsana urban block, Gujarat: Effect of groundwater induced aquifer compaction. Materials Today: Proceedings, 48, 1217–1223. doi:10.1016/j.matpr.2021.08.254.

[52] Cigna, F., & Tapete, D. (2022). Land Subsidence and Aquifer-System Storage Loss in Central Mexico: A Quasi-Continental Investigation with Sentinel-1 InSAR. Geophysical Research Letters, 49(15). doi:10.1029/2022GL098923.

[53] Liu, R., Zhao, Y., Cao, G., Wang, Q., Ma, M., Li, E., & Deng, H. (2022). Threat of land subsidence to the groundwater supply capacity of a multi-layer aquifer system. Journal of Hydrology: Regional Studies, 44, 101240. doi:10.1016/j.ejrh.2022.101240.

[54] Akitaya, K., & Aichi, M. (2023). Land subsidence caused by seasonal groundwater level fluctuations in Kawajima (Japan) and one-dimensional numerical modeling with an evolutionary algorithm. Hydrogeology Journal, 31(1), 147–165. doi:10.1007/s10040-022-02566-6.

[55] Saudi Vision 2030. (2026). Saudi Arabia Vision 2030 Website. Saudi Vision 2030, Saudi Arabia, Riyadh. Available online: https://www.vision2030.gov.sa/en (accessed on April 2026).

[56] Adem, E., Elfeki, A., Chaabani, A., Alwegdani, A., Hussain, S., & Elhag, M. (2024). Impact of satellite precipitation estimation methods on the hydrological response: case study Wadi Nu'man basin, Saudi Arabia. Theoretical and Applied Climatology, 155(5), 3907-3925. doi:10.1007/s00704-024-04855-4.

[57] Copernicus. (2026). Conventional Data Access Hubs. European Commission, Brussels, Belgium. Available online: https://www.copernicus.eu/en/access-data/conventional-data-access-hubs (accessed on April 2026).

[58] USGS. (2026). USGS EarthExplorer. United States Geological Survey, Virginia, United States. Available online: https://earthexplorer.usgs.gov/. (accessed on April 2026).

[59] ASF. (2025). Alaska Satellite Facility (ASF). University of Alaska Fairbanks, Alaska, United States. Available online: https://asf.alaska.edu/. (accessed on April 2026)

[60] Miky, Y. (2019). Multitemporal Sentinel-1SAR Interferometry for Surface Deformation Monitoring near High Dam in Aswan, Egypt. American Journal of Geographic Information System, 8(2), 96–102. doi:10.5923/j.ajgis.20190802.05.

[61] Khan, S., Waseem, M., & Khan, M. A. (2021). A Seismic Hazard Map Based on Geology and Shear-wave Velocity in Rawalpindi–Islamabad, Pakistan. Acta Geologica Sinica (English Edition), 95(2), 659–673. doi:10.1111/1755-6724.14405.